Time-domain study of surface plasmon polariton propagation in silver nanowires

Wenhua Zhao [1,2,*] Álvaro Rodríguez Echarri [1] Alberto Eljarrat [3,4] Hannah C. Nerl [3] Thomas Kiel [2] Benedikt Haas [3,4] Henry Halim [5] Yan Lu [5,6] Christoph T. Koch [3,4,†] and Kurt Busch [2,1,‡]

[1] *Max-Born-Institut, 12489 Berlin, Germany*

[2] *Department of Physics, AG Theoretische Optik & Photonik, Humboldt-Universität zu Berlin, 12489 Berlin, Germany*

[3] *Department of Physics, Structure Research and Electron Microscopy group, Humboldt-Universität zu Berlin, 12489 Berlin, Germany*

[4] *Center for the Science of Materials Berlin, Humboldt-Universität zu Berlin, 12489 Berlin, Germany*

[5] *Helmholtz-Zentrum Berlin for Materials and Energy, 14109 Berlin, Germany*

[6] *Friedrich-Schiller-University, 07737 Jena, Germany*

(Received 6 November 2025; accepted 15 January 2026; published 18 February 2026)

Electron microscopy techniques such as electron energy-loss spectroscopy (EELS) facilitate the spatiospectral characterization of plasmonic nanostructures. In this work, a time-dependent perspective is presented that significantly enhances the utility of EELS. In particular, this approach facilitates the analysis of the dynamics of plasmonic excitations that repeatedly interact with swift electrons in a STEM-EELS configuration. This includes the bulk plasmon mode, which can only be excited by penetrating electron beams, and the fundamental surface plasmon polariton modes propagating along the wire, which can be excited by both penetrating and aloof trajectories. In addition, the role of higher-order azimuthal surface plasmon polariton modes, often overlooked for very thin wires, is observed and analyzed in both the energy-loss spectrum and from the dynamical perspective. Such a complete understanding of the interaction of electrons and plasmonic excitations is key for the design of efficient plasmonic sensors, the study of hot electron dynamics in metals, and applications in the context of electron quantum optics, where full control of the spatial and temporal characteristics of the fields at the nanometer and femtosecond scales is highly desirable.

DOI: 10.1103/gpqj-4v29

I. INTRODUCTION

The understanding of light-matter interaction at the nanoscale is a fundamental area of research that drives advances in a wide range of applications. In this context, the collective oscillations of conduction electrons in metals, the so-called plasmons (volume plasmons or, when spatially constrained by a material interface, surface plasmons), have proven to exhibit extraordinary properties that can be employed to boost light-matter interaction [1–3] for applications in circuitry [4,5], sensing [6–8], quantum optics [9,10], quantum information [11], and nonlinear optics [12]. This is facilitated via the formation of hybrid light-matter excitations, the so-called plasmon polaritons, which come in the form of surface waves that propagate along dielectric-metal interfaces (surface plasmon polaritons) or are associated with geometry-induced and spatially localized resonances (particle plasmon polaritons, also known as localized surface plasmon polaritons) [13]. Amongst the most common plasmonic materials, silver provides the lowest intrinsic losses, leading to higher-quality factors of resonances [14]. In addition, self-assembled high-quality silver nanowires exhibit exceptionally smooth surfaces and therefore facilitate the propagation of surface plasmon polaritons for long distances [15–17]. This provides an ideal illustrative system for our combined experimental-theoretical analyses of these plasmonic excitations and their dynamics.

To excite and study plasmonic excitations, the use of swift electrons as in electron energy-loss spectroscopy (EELS) [18] or cathodoluminescence (CL) [19] allows for probing plasmonic resonances with nanometer spatial resolution while simultaneously providing meV energy resolution [20–22]. As a matter of fact, EELS and CL have successfully been employed to study plasmonic excitations in metals for several decades [23–28].

Conventional experimental and/or theoretical/numerical analyses of EELS for plasmonic systems provide information about the spectral position and localization in real space of resonances. As a result, direct information on the actual time dependence of the interaction processes between the electron beam and the different plasmonic excitations is not available. However, this missing temporal component is essential for developing a more intuitive and complete understanding of the energy-loss and -gain mechanisms that are at work. Indeed, the interactions that occur between the sample and the electron beam while the beam electrons approach, pass by, or traverse the sample ultimately lead to the overall energy loss experienced by the electron beam, i.e., the resulting spectra.

*Contact author: wzhao@physik.hu-berlin.de
†Contact author: christoph.koch@hu-berlin.de
‡Contact author: kurt.busch@physik.hu-berlin.de

Published by the American Physical Society under the terms of the Creative Commons Attribution 4.0 International license. Further distribution of this work must maintain attribution to the author(s) and the published article's title, journal citation, and DOI.

Recent experimental study [29] reports the visualization of the near-field dynamics via a focused continuous-wave laser and ultrashort electron pulses, where attosecond-resolved dipole and quadrupole distributions in a slit resonator are shown. Therefore, a detailed understanding of such interactions and their dynamics is of paramount importance for the full utilization of plasmonic nanostructures to control/enhance physical processes in their vicinity.

Here, we present a thorough time-domain study for the interaction between the electron and the induced fields by solving the time-dependent Maxwell's equations. Based on the well-established EELS theory [18,30–32] and its experimental observation, we obtain the classical coupling efficiency between the electron and the plasmonic nanoparticle, with which we unveil the temporal interaction dynamics via Fourier transform (FT) techniques. This study relies on the combination of the unprecedented high energy resolution of modern electron microscopes and a highly efficient time-domain simulation approach to solve the full electromagnetic problem. Thereby, we characterize the dynamics of the associated plasmonic excitations. Moreover, we provide a comprehensive approach for the description of propagating surface plasmon polaritons (SPPs) in long nanowires along with a detailed understanding of the dynamics underlying the conventional electron energy-loss (EEL) spectra. Finally, we reveal the role of the often neglected higher-order azimuthal modes (higher-order SPPs) in the obtained EELS signals.

II. RESULTS AND DISCUSSION

To fully understand the SPP dynamics, we have combined experimental and theoretical studies. First, in the experimental setup (see Fig. 1), we consider a swift electron beam interacting with a long silver nanowire with a few microns in length and a few tens of nanometers in diameter, which was placed on a thin silicon nitride substrate. We acquired the corresponding spatiospectral EELS maps using a state-of-the-art scanning transmission electron microscope (STEM) (for details, see Secs. III A and III B).

To complement the measurements, we have performed corresponding numerical computations by solving Maxwell's equations using the discontinuous galerkin time-domain (DGTD) finite-element method [33–35], which facilitates the spatiotemporal resolution of the plasmonic modes in the nanometer and femtosecond range (for details, see Sec. III C). We modeled the material properties of a free-standing silver nanowire of radius R and length L using a local Drude permittivity $\epsilon(\omega) = \epsilon_\mathrm{b} - \omega_\mathrm{p}^2/\omega(\omega + \mathrm{i}\gamma)$ with bulk plasmon energy $\hbar\omega_\mathrm{p} = 9.17\,\mathrm{eV}$, damping constant $\hbar\gamma = 21\,\mathrm{meV}$, and $\epsilon_\mathrm{b} = 1$ [36] [see Sec. S5 in Supplemental Material (SM) Ref. [37] for a comparison of the Drude material model with measured optical data and a discussion of the effects of electronic interband transitions].

The presentation of the discussion is organized as follows. In Sec. II A, we revisit the theory of electron energy-loss spectroscopy and introduce the classical coupling efficiency together with its time-domain Fourier transform. To elucidate the temporal dynamics of surface plasmon polariton (SPP) excitations, we first present the time-dependent induced fields obtained directly from DGTD simulations in Sec. II B, where we define the round-trip and return times of the plasmonic fields. Using these induced fields, we then perform numerical EELS calculations and compare the results with experimental EELS maps in Sec. II C. Subsequently, we analyze the excitation amplitude dynamics through the Fourier transform of the coupling efficiency and discuss the emergence of higher-order azimuthal modes. Finally, in Sec. II D, we provide a simplified interpretation of the complex dynamics revealed in Secs. II B and II C, describing them as a superposition of fundamental SPP modes.

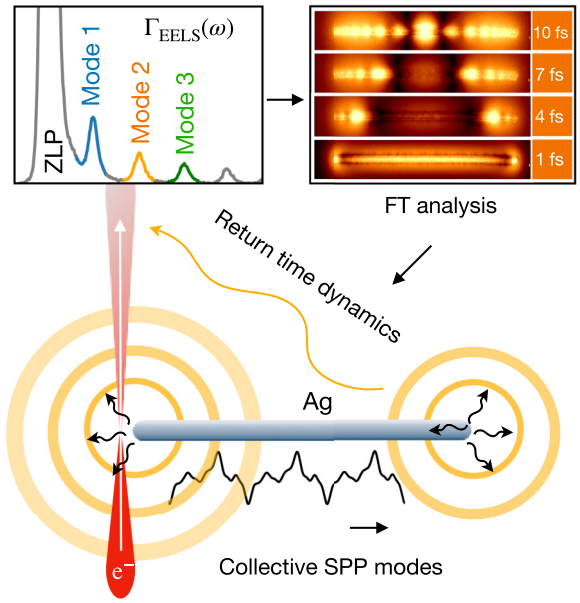


FIG. 1. From electron energy loss to the plasmonic excitation amplitude. Illustration of electron energy-loss spectroscopy in STEM configuration. While an electron beam passes in close proximity to the plasmonic silver nanowire (so-called aloof trajectory), it excites surface plasmon polaritons (SPPs) that propagate down the wire (see black curves manifesting the collective SPP modes). Based on the resulting interactions of these induced plasmonic fields with the electron beam, the latter loses energy. Inside the electron microscope's spectrometer, the individual electron energies are analyzed, leading to loss spectra that feature peaks in the intensity count that are associated with different SPP modes. Through a Fourier transform (FT), we obtain the time evolution of the energy loss $|\tilde{\eta}_\mathrm{r}(t)|$ in Eq. (7), where four snapshots display its magnitude at different times $t = 1, 4, 7$, and 10 fs ($t = 0$ corresponds to the time when the electron beam arrives at the nearest proximity to the nanowire). Analogous considerations can be applied to penetrating trajectories, where, however, additional plasmonic excitations such as bulk plasmons have to be considered.

A. Analytics: electron energy-loss spectroscopy

On one hand, in a classical picture, the energy loss ΔE experienced by a swift electron that moves at velocity $\mathbf{v}$, originates from the backaction of the induced fields on the electron and reads [30,31,38]

$$\Delta E = e\int dt\,\mathbf{v}\cdot\mathbf{E}^{\mathrm{ind}}[\mathbf{r}_e(t),t] \tag{1}$$

$$= \frac{e}{2\pi}\int_{-\infty}^{\infty} d\omega \int_{-\infty}^{\infty} dz E_z(z,\omega) e^{-i\omega\frac{z-z_0}{v}}. \tag{2}$$

Here, $-e < 0$ is the electron charge. Assuming that the electron is moving in the z direction, the position of the electron at time t is $\mathbf{r}_e(t) = (x_0, y_0, z_0 + vt)$, with (x_0, y_0) denoting the electron trajectory position in the xy plane and v denoting the velocity of the electron, where we adopt the no-recoil approximation [31]. For aloof trajectories, the impact parameter $b \equiv |y_0| - R$ gives the shortest distance between the electron trajectory and the surface of the wire. Further, we define the classical frequency-domain coupling efficiency as

$$\eta(\omega) = \frac{e}{2\pi\omega}\int_{-\infty}^{\infty} dz E_z(z,\omega) e^{-i\omega\frac{z-z_0}{v}} \equiv \eta_r(\omega) + i\eta_i(\omega), \tag{3}$$

which encodes spectral overlap between induced fields and electron motion, per angular frequency.

On the other hand, in a semiclassical picture, we can write the energy loss experienced by the electron as

$$\Delta E = \int_0^{\infty} d\omega\, \hbar\omega\, \Gamma_{\mathrm{EELS}}(\omega), \tag{4}$$

which is the well-known loss probability in units of transferred frequency $\omega > 0$ (i.e., associated with an energy loss $\hbar\omega$). Note that E_z^{ind} denotes the induced electric field's z component along the electron trajectory, and the integral extends over the entire trajectory. Via the complex-valued coupling efficiency with real-valued contributions $\eta_r(\omega)$ and $\eta_i(\omega)$, we then obtain

$$\Gamma_{\mathrm{EELS}}(\omega) = \frac{2}{\hbar}\eta_r(\omega) \quad \text{for } \omega > 0. \tag{5}$$

The real part $\eta_r(\omega)$ governs the dissipative processes, which originates from the in-phase oscillation between the induced fields and the motion of the electron, thus providing information about the net energy exchange of the induced fields (which encodes the plasmonic response) with the electron. While $\eta_r(\omega)$ corresponds to the EELS probability [Eq. (5)] that can be measured in experiments, the imaginary part can be obtained from the Kramers-Kronig relation [39] by exploiting the causality and analyticity of $\eta(\omega)$ [see more details in Sec. S1 of SM Ref. [37] (see also Refs. [30,31,40] therein)]. Note that $\eta_r(\omega)$ is odd and $\eta_i(\omega)$ is even in ω [i.e., $\eta(-\omega) = -\eta^*(\omega)$], and therefore, its Fourier transform in time is an imaginary quantity

$$\tilde{\eta}(t) = \int_{-\infty}^{\infty} \frac{\mathrm{d}\omega}{2\pi}\,\eta(\omega)\,\mathrm{e}^{-\mathrm{i}\omega t} = \mathrm{i}[\tilde{\eta}_r(t) + \tilde{\eta}_i(t)], \tag{6}$$

where $\tilde{\eta}_r(t)$ is obtained from $\eta_r(\omega)$, and $\tilde{\eta}_i(t)$ from $\eta_i(\omega)$. Both components are real-valued and, as discussed below, carry information about the light-matter interaction, and they describe the temporal dynamics of the system.

By considering the Fourier transform of $\eta_r(\omega)$, we obtain

$$\tilde{\eta}_r(t) = -\frac{e}{4\pi}\int_{-\infty}^{\infty}\mathrm{d}z \int_{t'-t}^{t'+t}\mathrm{d}\tau\; E_z^{\mathrm{ind}}(z,\tau), \tag{7}$$

where $t' = (z - z_0)/v$ denotes the arrival time of the electron at position z. Instead of integrating the electric field along the electron trajectory as in Eq. (5), in this expression, for each position z, we integrate over a temporal window of width $2t$ centered around the arrival time t' (see details in Sec. S1 of SM Ref. [37]). This indicates that $\tilde{\eta}_r(t)$ captures the immediate excitation amplitude dynamics that is dominated by the direct energy transfer from the electron to the plasmonic excitations (i.e., the near-field interaction). Consequently, this is what is measured in the direct EELS experiment. Similarly, we calculate the second term $\tilde{\eta}_i(t)$ (see details in SM Ref. [37]), which indicates how much of the plasmonic energy remains stored in the system or is attenuated (radiatively or nonradiatively) after the main interaction time, thus being related with the collective plasmonic quality factor [14,41].

It is important to emphasize that the Fourier transform itself does not introduce new information. However, by starting from the experimentally measured EELS probability, we can reconstruct the full complex coupling efficiency $\eta(\omega)$ through the Kramers–Kronig relation, thereby enabling access to the corresponding time-domain dynamics.

In the remainder of this work, we focus on $\tilde{\eta}_r(t)$, derived from measured and simulated $\Gamma_{\mathrm{EELS}}(\omega)$, capturing the dynamics of the direct interaction between beam electrons and the nanowire. Nonetheless, we emphasize the potential of further exploring $\tilde{\eta}_r(t)$ in the time domain. For example, one may investigate $\tilde{\eta}_i(t)$ or the time derivative of $\tilde{\eta}_r(t)$, which corresponds to the Fourier transform of $\propto \hbar\omega\eta_r(\omega)$ and provides access to the direct (retarded) electric field induced by the electron. Various strategies can therefore be employed to extract time-domain information from spectral data. This is possible because the Fourier transform is not applied to an arbitrary function, but to one that exhibits well-defined physical properties such as causality and analyticity, as previously discussed. Our analysis operates in the single-electron, linear-response regime, with post-selection on electrons that have lost energy $\hbar\omega$. In a full quantum treatment, the joint electron–SPP state yields the loss probability via Fermi's Golden Rule [31,42]. Here we use a classical, channel-resolved coupling efficiency that is causal (i.e., obeys the Kramers–Kronig relation) and whose real part is defined to correspond directly to the measured loss probability [42]. Multi-electron or multiplasmon processes would require higher-order terms and lie beyond the scope of our work. Remarkably, this enables us to probe the nanoscale light–matter interaction dynamics (i.e., in the near field) by measuring the electron long after its interaction with the plasmonic structure (i.e., in the far field).

B. Numerics: time domain dynamics via DGTD

One of the main advantages of the DGTD approach to solving Maxwell's equations is that we obtain the time-dependent induced fields $\mathbf{E}^{\mathrm{ind}}(\mathbf{r}, t)$, which allows for studying the dynamics of the entire system time step by time step. Along these lines, we performed numerical computations for a long silver nanowire (length $L = 1.2\,\mu$m, radius $R = 15$ nm, terminated by hemispherical caps) excited by a swift electron with velocity $v = 0.4c$ ($\approx$47 keV) and impact parameter $b = 5$ nm, so that the electron passes by the nanowire in about a tenth of a femtosecond, therefore defining the time when the electron is at the closest approach as $t = 0$.

In Figs. 2(a)–2(c), we display, on a logarithmic scale, the magnitude of the induced electric field $|\mathbf{E}^{\mathrm{ind}}(\mathbf{r}, t)|$ in the xz plane for different instances of time and for the specific electron trajectory with $x_0 = 0.36\,\mu$m and impact parameter

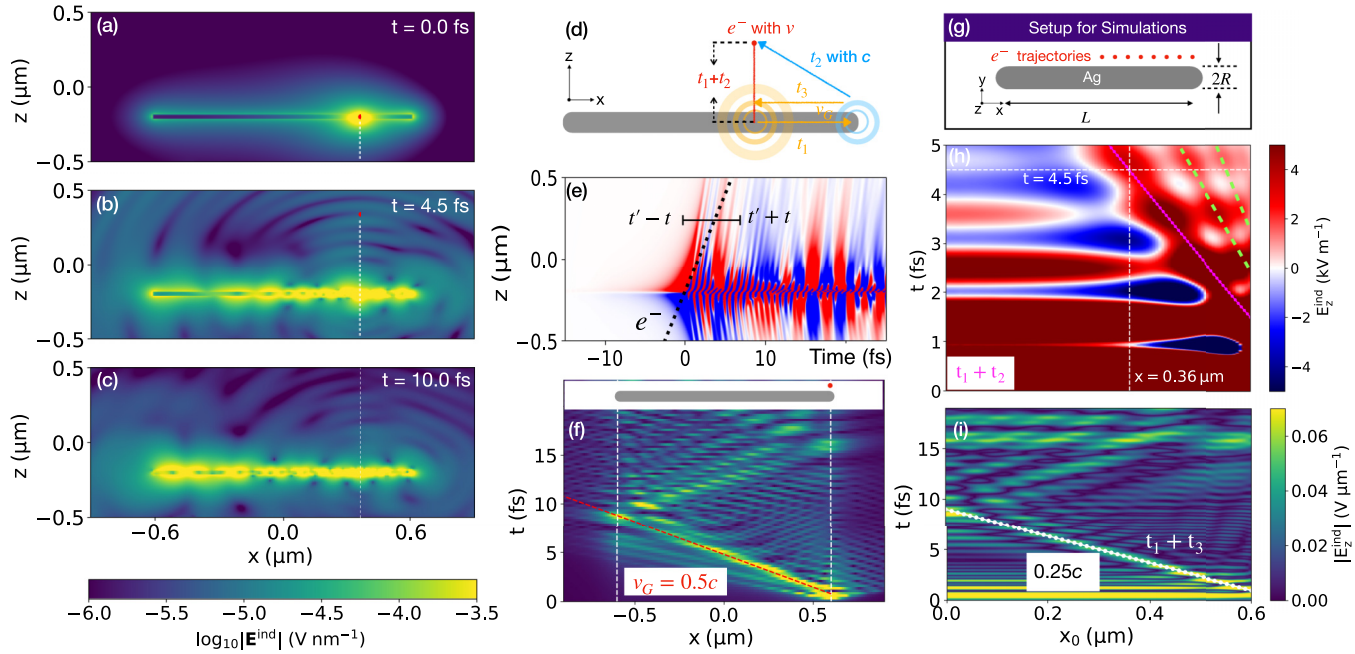


FIG. 2. Theoretical interpretation of the temporal EELS signal. Snapshots at different times of the induced electric field for a swift electron beam traveling with velocity $v = 0.4c$ (kinetic energy ≈47 keV): (a) right after arriving at the silver nanowire of $R = 15$ nm and $L = 1.2$ μm, (b) after passing the wire, and (c) leaving the computational domain (see exact times in the insets). (d) Schematic of the return time dynamics (see the main text for details). (e) Time-resolved induced electric field $E_z^{\rm ind}(z, t)$ along the electron trajectory (velocity $v = 0.4c$ at $x_0 = 0.36$ μm). The black dotted lines indicate the position of the electron in space and time. Around $t \approx 0$ fs, the electron arrives at the point of closest approach to the nanowire. We further show the time window $[t' - t, t' + t]$ appearing in the time integral of Eq. (7). (f) Induced electric field amplitude along the x axis of the nanowire for an electron beam passing aloof at the right edge ($x_0 = L/2$ and $y_0 = 20$ nm). (g) Sketch of the system for numerical computations, where a free-standing silver nanowire was considered. The electron trajectories in the xy plane are marked as red dots, where the electrons travel in the z direction. (h) Induced electric field at the position of the electron for different electron trajectories given in (g), together with the return time $t_1 + t_2$ (pink curve). For the same system, we show in (i) the induced electric field $|E_z^{\rm ind}(\mathbf{r}_s, t)|$ near the surface of the nanowire (i.e., $\mathbf{r}_s = [x_0, R + b, z_s]$) for different trajectories, where $R < z_s < 2\pi c/\omega_{\rm p}$ within the near-field region. The white-dotted line indicates the SPP round-trip time $t_1 + t_3$ using the group velocity $v_G \approx 0.5c$.

$b = 5$ nm. In each graph, the instantaneous position of the electron $\mathbf{r}_e(t)$ is indicated by a red dot. The electron reaches the center of the nanowire around time $t \approx 0$ fs, leading to large field values around the nearest point between the nanowire and the electron [see Fig. 2(a)]. This corresponds to the excitation of SPP wave packets that propagate along either side of the nanowire, see Fig. 2(b). In the meantime, the electron has moved further away from the nanowire and experiences the scattered field from the previous instances in time (note the presence of wavefront fringes). For this specific example, the SPP wave packet that moves to the right reaches the nanowire's right cap before the left-moving SPP wave packet reaches the left cap. When such a right-moving SPP wave packet reaches the cap, it is scattered, and a spherical-like radiation burst is emitted. This burst travels at the speed of light in vacuum so that parts of it catch up and interact with the slower-moving electron. Roughly, it is at time $t \approx 4.5$ fs that the first wavefront of the radiation burst reaches the electron, which is clearly seen in the video (see Sec. S10 in SM Ref. [37]). Later, when the electron has already left the computational domain, we observe that the SPP wave packet moving to the left reaches the left cap, again leading to the emission of a radiation burst which, relative to the first burst, is delayed by about ∼8 fs. The resulting wave fronts interfere with the rest of the electromagnetic fields [Fig. 2(c)]. Through the snapshots of Figs. 2(a)–2(c), we study the field strength that the electron experiences when traveling along its trajectory. Interestingly, the cap-related EELS effect is a consequence of the finite length of the wire, and the underlying mechanism is illustrated in Fig. 2(d). Specifically, when the electron meets the nanowire, the excited SPP wave packet moves with group velocity v_G to the right cap during a time t_1, then the right cap starts to radiate. The resulting wavefronts travel at the speed of light c in vacuum, and after time t_2 they reach the electron [see the field experienced by the electron depicted in Fig. 2(e)]. Simultaneously, the electron travels at $v = 0.4c$ for a time $t_R = t_1 + t_2$, which we define as *return time*, which is the time it takes for the initial excitation at $t = 0$ to reach the electron again. The return time is calculated using the Pythagorean theorem as

$$v^2(t_1 + t_2 + \Delta)^2 + t_1^2 v_G^2 = t_2^2 c^2. \tag{8}$$

Here, Δ denotes a small delay between the arrival time of the electron at the center of the nanowire and the time at which the SPP wave packets start to propagate due to the retardation that is required to build up the material response.

To determine the group velocity v_G of the excited SPP wave packets in the wire, we depict in Fig. 2(f) the electric field $|\mathbf{E}^{\rm ind}|$ as a function of time along a line parallel to the nanowire in the x direction when the electron is very close

to the right cap ($x_0 = 0.6$ μm, impact parameter $b = 5$ nm, see upper inset). The two vertical dashed white lines at $x = \pm 0.6$ μm indicate the caps of the nanowire. Around $t \approx 0$ fs, the electron arrives at the point of minimal distance to the nanowire, and we observed that a SPP wave packet starts to travel from the right to the left side with a group velocity of $v_G \approx 0.5c$ as determined by fitting the slope (red dashed curve). We found the resulting group velocity to be dependent of the radius of the wire, which influences the SPP dispersion relation. However, the group velocity's value is independent of the nanowire length and the electron's kinetic energy. For further details, we refer to Fig. S6 in SM Ref. [37], where we depict v_G for different parameters (i.e., electron kinetic energy, radius, and length of the nanowire). Note that, due to the delayed material response and the finite impact parameter, the resulting SPP wave packet requires about $\Delta \sim 1$ fs to form. Moreover, after the main SPP wave packet has formed, there are additional smaller satellite packets moving with slower velocities. However, due to the interference of all these satellite features, a rather complex dynamics results. In other words, all SPP modes are excited at once and propagate together in an intricate manner, which we analyze more closely in Sec. II D and Sec. 9 in SM Ref. [37] (see also Refs. [43–45] therein). Also, less intense features (below the main propagating feature) that move at the speed of light are visible, which corresponds to the induced field originating at the nearest cap moving in free space.

As shown in Eq. (5), in order to calculate $\Gamma_{\mathrm{EELS}}(\omega)$, we need to compute $E_z^{\mathrm{ind}}(z,\omega)$, which is the Fourier transform of the z component of the time-dependent induced electric fields $E_z^{\mathrm{ind}}(z,t) = \hat{\mathbf{z}} \cdot \mathbf{E}^{\mathrm{ind}}$ that can be directly recorded by the DGTD computations along the electron trajectory. For instance, in Fig. 2(e), we depict the electric field $E_z^{\mathrm{ind}}(z,t)$ induced by an electron moving at velocity $\boldsymbol{v} = 0.4c\,\hat{\mathbf{z}}$ on an aloof trajectory with $x_0 = 0.36$ μm. The black-dotted line indicates the position of the electron (in space and time) when it traverses the computational domain. When moving along its trajectory, the electron experiences an accelerating/decelerating force depending on the sign of the field (cf. the colored red-blue scale). Note that while the overall effect of the induced electric field acting on the electron leads to a net energy loss, there are positions/times on the trajectory where the electron experiences a differential gain. Overall, the induced field does work against the electron. In Fig. 2(e), we further display the time window $[t'-t, t'+t]$ required to evaluate the time integral in Eq. (7). Note that the window is centered around the arrival time t' of the electron at position z.

Based on the fitted group velocity and using Eq. (8), we depict in Fig. 2(h) the electric field at the position of the electron for different trajectories [i.e., for different x_0 with fixed impact parameter $b = 5$ nm, as shown in Fig. 2(g)], where the return time $t_R = t_1 + t_2$ of the first bright SPP wave packet is superimposed (pink curve). We notice an excellent match between the strong enhancement of the electric field at the position of the electron and the return time t_R, in agreement with the scheme of Fig. 2(d). The features of lower intensity, denoted with green dashed lines in the right top corner of Fig. 2(h), originate from the aforementioned SPP satellites. Note that for the trajectory $x_0 = 0.36$ μm, we also highlight the time $t = 4.5$ fs (white dashed lines), corresponding to the time in Fig. 2(b), where we observe a strong enhancement of the electric field at the electron position. Hence, such a strong enhancement is due to the interaction of the scattered field of the propagating SPP wave packet that originates at the right cap of the wire. The graph in Fig. 2(i) shows the electric near-field $E_z^{\mathrm{ind}}(\mathbf{r}_s, t)$ at the position near the surface of the wire at different electron trajectories (i.e., $\mathbf{r}_s = [x_0, R+b, z_s]$, where $R < z_s < 2\pi c/\omega_{\mathrm{p}}$).

In fact, when the SPP wave packet traveling to the right reaches the cap of the nanowire, it is not completely converted into radiation. Rather, a portion of the electromagnetic energy remains within the nanowire in form of a reflected SPP wave packet that moves along the wire to the left, as shown in the scheme of Fig. 2(d). This effect is further supported by the study of the experimental and theoretical EELS profiles of different modes in Sec. S2, Fig. S2(d) (experiment) and Fig. S3(b) (theory) of SM Ref. [37] (see also Refs. [38,46] therein), where all modes exhibit a partial drop in EELS intensity, indicating that, at the wire caps, a fraction of the energy of the mode is reflected back and remains in the wire, and the rest is transmitted, thus leaving the wire and radiating away into free space. To characterize the associated time dynamics, we define the *round-trip time* $t_1 + t_3 \approx 2t_1 = 2(L/2 - |x_0|)/v_G$, which is the time the excited SPP wave packet requires to travel to the right cap and return to its launch point x_0. Furthermore, the electric near-field dynamics and this round-trip time are closely connected with the EELS signal, which we will discuss in the next section.

C. Experiment and DGTD: azimuthal modes and the excitation dynamics

As demonstrated in Fig. 1, $\tilde{\eta}_{\mathrm{r}}(t)$ provides us with temporal information regarding the excitation amplitude of the plasmonic excitations associated with the nanowire. In this figure, we depict the amplitude of $|\tilde{\eta}_{\mathrm{r}}(t)|$ as a function of space (i.e., different electron trajectories) and time, thereby creating characteristic maps of the excitation amplitude. Despite the fact that the electron is detected far from the interaction region, the information we obtain is directly related to the electric near-field distribution [48], as we demonstrate below.

Chemically synthesized silver nanowires, owing to their reduced dimensionality, low intrinsic losses, and exceptionally smooth surfaces, constitute an excellent platform for investigating propagating surface plasmon polaritons (SPPs). Figure 3(a) shows an experimental electron energy-loss (EELS) line scan acquired for a long silver nanowire ($L \approx 2.6$ μm, $R \approx 30$ nm) using aloof electron trajectories with an impact parameter of $b \approx 5$ nm from the wire surface. The corresponding dispersion relation, obtained from the spatial Fourier transform of the EELS data along the wire axis, is presented in Fig. 3(b). The temporal evolution of the excitation amplitude, retrieved from the temporal Fourier transform of the same dataset, is shown in Fig. 3(c). The structural context of these measurements is provided by the high-angle annular dark-field (HAADF) image [49] in Fig. 3(d), which displays the nanowire and the trajectory positions. The corresponding experimental measurements for this figure were performed with a 200 keV electron beam ($v \approx 0.7c$). To evaluate the

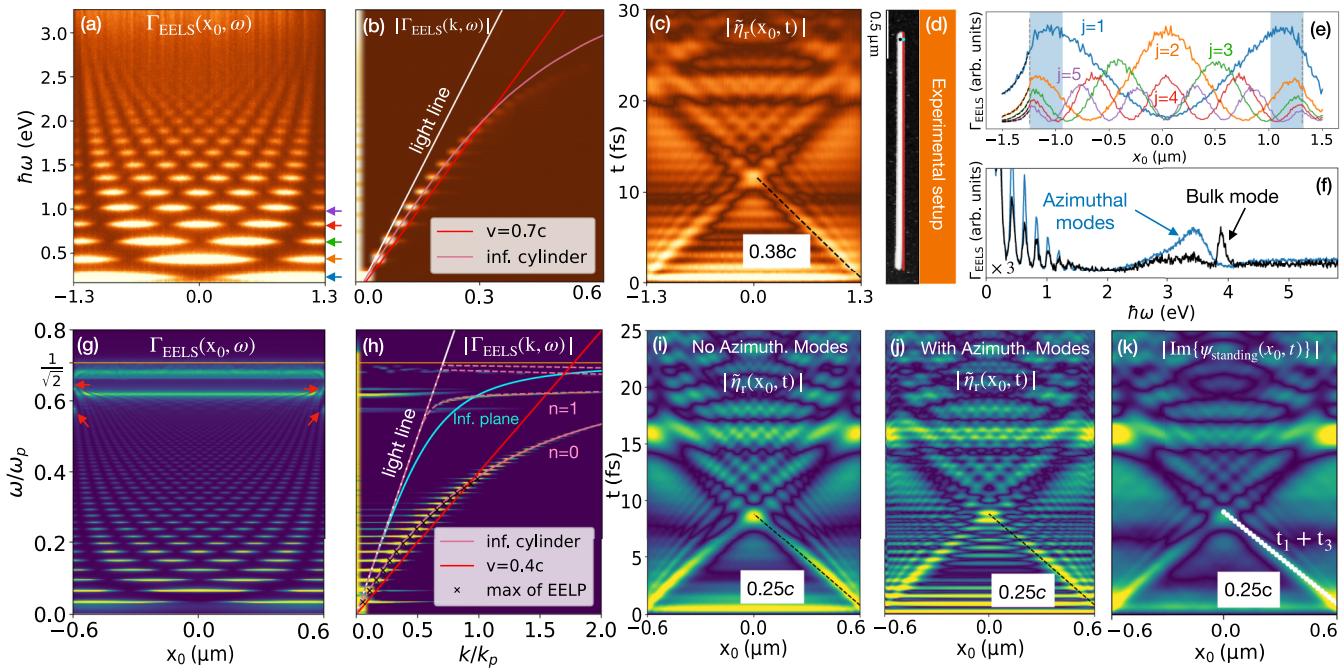


FIG. 3. Spatiotemporal characterization of plasmonic excitations in silver nanowires induced by a beam of swift electrons: experiments and computations. (a) *(Experiment)* EELS line scan showing the electron energy loss (vertical axis) as a function of position (horizontal axis), acquired along the red line in (d) for a silver nanowire of length ∼2.6 μm and radius ∼30 nm, excited by aloof electron beams with a kinetic energy of 200 keV at a distance of ∼5 nm from the wire surface. (b) *(Experiment)* Dispersion relation obtained from the spatial Fourier transform of (a) along the x axis, shown together with that of an infinite silver cylinder of radius 30 nm calculated using measured optical data (pink curve) [36]. The electron-line dispersion (red) and the light line (white) are plotted in units of $k_p = \omega_p/c$, where $\hbar\omega_p = 9.17\,\text{eV}$ is the plasma energy of silver within the Drude model. (c) *(Experiment)* Amplitude of $\tilde{\eta}_r(t)$, obtained as the temporal Fourier transform of panel (a), representing the time evolution of the EELS signal for each electron trajectory. The slope of the feature propagating toward the center corresponds to a velocity of ∼0.38c (black dashed line). (d) *(Experiment)* High-angle annular dark-field (HAADF) image of a silver nanowire of length ∼2.6 μm and radius ∼30 nm. (e) *(Experiment)* Intensity profiles of the EELS peaks for trajectories along the red line in (d) ($b \approx 5$ nm), corresponding to different plasmonic modes (see colored arrows in (a)). The two vertical grey dashed lines mark the ends of the nanowire. The black dashed lines outside the nanowire are exponential fits describing the decay of the signal in the surrounding region. (f) *(Experiment)* Blue line: EEL spectrum for the aloof trajectory indicated by the blue point in (d), showing the presence of higher-order azimuthal SPP modes. Black line: EEL spectrum for the penetrating trajectory indicated by the black point in (d), showing the bulk plasmon mode. *Note:* the intensity of the black curve is multiplied by a factor of three to emphasize the bulk plasmon peak. (g) *(Theory)* Spatially resolved EELS map for the system shown in Fig. 2(g), calculated using DGTD for a silver nanowire of length ∼1.2 μm and radius ∼15 nm, modeled with a local Drude permittivity and $\varepsilon_b = 1$. The orange line marks the surface plasmon resonance at $\omega/\omega_p = 1/\sqrt{2}$. The two bright modes below the orange line correspond to higher-order azimuthal modes. (h) *(Theory)* Dispersion relation obtained from the spatial Fourier transform of (g) along the x axis, together with the analytical result for an infinite silver cylinder of radius 15 nm using the Drude model (pink curve) [47], the electron-line dispersion (red), and the light line (white) in units of $k_p = \omega_p/c$. (i) *(Theory)* Amplitude of $\tilde{\eta}_r(t)$, the temporal Fourier transform of panel (g) without azimuthal modes. The main feature traveling from the tip to the center exhibits a slope of ∼0.25c (fitted black dashed line), corresponding to the SPP round-trip time $t_1 + t_3$ defined in the main text. Simulation results for a wire of radius $R = 30$ nm are provided in Fig. S4 of SM Ref. [37]. (j) *(Theory)* Same as (i), but including azimuthal modes. (k) *(Theory)* Superposition of standing waves computed from $\psi_{\text{standing}}(x,t) = \sum_j \hat{A}_j \cos^2(k_j x)\, e^{-i\omega_j t}$ for different modes, together with the SPP round-trip time $t_1 + t_3$. For simplicity, the color bars have been omitted. In all graphs, dark colors represent low values, while light colors represent high values (all graphs are shown on a linear scale).

influence of electron velocity, additional experiments were carried out at 30 kV and 60 kV acceleration voltages, yielding comparable results. This indicates that the main EELS features are largely independent of the electron velocity.

At first, we note that the experimental dispersion in Fig. 3(b) matches well with the analytical dispersion (pink curve) of an infinite silver cylinder using measured optical data for silver [36], where the desired relationship between the frequency ω and the wavenumber k is obtained by solving Maxwell's equations in the two different media while applying boundary conditions at the interfaces [38,47]. The corresponding analytical expression is given in Sec. S3 in SM Ref. [37]. Thus the experimentally measured wire can be considered to be sufficiently long so that its dispersion relation depends only on the radius and the material properties. Further, while in Fig. 1, we have shown snapshots of excitation amplitude for the entire region of interest (in the xy plane), in Fig. 3(c), we show the results corresponding to the electron

beam positions indicated by the red line in Fig. 3(d). For the full video in the xy plane, we refer to Sec. S10 in SM Ref. [37]. The experimental dispersion and dynamics of the excitation amplitude allow for comparison with numerical results, which we present below.

For the analysis presented in Fig. 3, we selected one specific experimental dataset that offers superior energy sampling within a narrower energy range compared with the other measurements. For completeness, additional datasets acquired with a 200 keV electron beam and covering a broader energy range are provided in Fig. S2 of SM Ref. [37], where the measured EELS maps for both aloof and penetrating trajectories are shown. These maps enable a direct comparison of the relative contributions from the bulk plasmon and the higher-order azimuthal SPP modes. The bulk plasmon, being a collective electronic excitation with a negligible associated electric field, can be efficiently excited only by electron trajectories that penetrate the silver nanowire. In contrast, the fundamental and higher-order azimuthal SPP modes—hybrid light–matter excitations that lie energetically below the screened bulk plasmon energy—can be excited efficiently by both penetrating and aloof electron trajectories. In the case of our thin nanowires, the higher-order SPP modes form an energy band centered around $\hbar\omega \sim 3.6$ eV, which lies close to the surface plasmon energy. Further details are provided in Fig. S3(a) of SM Ref. [37] (see also Refs. [38,46] therein).

For the EELS map in Fig. 3(a), and both maps in Fig. S2 in SM Ref. [37], we observe the fundamental azimuthal modes with $n = 0$ in the low energy range (0–3 eV), which resemble standing waves trapped between the caps of the wire. Further, in Fig. 3(e), we plot the intensity profiles of the EELS peaks for different plasmonic modes [see colored arrows in Fig. 3(a)]. The spatial variations result from the interaction of the electron beam with the spatial profiles of the different plasmonic modes for which we provide more details in the following section and in Fig. S2 of SM Ref. [37].

To further distinguish between the higher-order azimuthal SPP modes and the bulk plasmon mode, Fig. 3(f) displays the EEL spectra corresponding to the aloof trajectory [blue point in Fig. 3(d)] and the penetrating trajectory [black point in Fig. 3(d)]. The associated full EELS maps for both cases are provided in Fig. S2 of SM Ref. [37]. For the aloof trajectory [blue curve in Fig. 3(f)], we observe a relatively broad peak centered around $\hbar\omega \sim 3.6$ eV, which arises from the higher-order azimuthal SPP modes with $n \geqslant 1$, lying below the screened surface plasmon energy [50] $\hbar\omega_{\mathrm{sp}}^{*} = \hbar\omega_{\mathrm{p}}/\sqrt{1 + \mathrm{Re}\{\epsilon_{\mathrm{b}}(\omega_{\mathrm{sp}}^{*})\}} \approx 3.67$ eV, where $\varepsilon_{\mathrm{b}}(\omega)$ is obtained from measured optical data [36] (see Fig. S5 in SM Ref. [37] for further details). Here, the superscript * denotes the screening effect on the surface plasmon energy. As the azimuthal order n increases, the corresponding modal wavelength decreases, and the curvature of the nanowire becomes less significant. Consequently, these higher-order modes approach the energy of a surface plasmon polariton supported by a planar metal-dielectric interface. They lie at higher energies than the fundamental ($n = 0$) mode and exhibit an azimuthal phase dependence $e^{in\varphi}$ around the nanowire axis. To date, such higher-order azimuthal modes have received little experimental attention; to the best of our knowledge, only Ref. [51] reported their observation via quantum-dot fluorescence imaging of silver nanowires with radii of about 150 nm. In contrast, the EEL spectrum for the penetrating trajectory [black curve in Fig. 3(f)] displays a sharp peak at the screened bulk plasmon energy [20,21,31], $\hbar\omega_{\mathrm{p}}^{*} = \hbar\omega_{\mathrm{p}}/\sqrt{\mathrm{Re}\{\epsilon_{\mathrm{b}}(\omega_{\mathrm{p}}^{*})\}} \approx 3.81$ eV, corresponding to the excitation of the collective bulk plasmon mode.

Similarly, for the EELS map with aloof trajectories [see Figs. 3(a) and S2(a)], we observe the appearance of higher-order azimuthal SPP modes around $\hbar\omega \sim 3.6$ eV. For penetrating trajectories in Fig. S2b, we observe the bulk plasmon peaks around $\hbar\omega \sim 3.8$ eV.

For reference, Fig. S3(c) in SM Ref. [37] shows the numerically computed EEL spectra, where the bulk plasmon peak appears only for the penetrating trajectory and is located precisely at the bulk plasmon energy predicted by the Drude model (i.e., $\hbar\omega_{\mathrm{p}} \approx 9.17$ eV). We note a discrepancy between the experimental and simulated bulk plasmon peak positions, which could be mitigated by incorporating measured optical data into the numerical calculations. This adjustment would account for the screening effects arising from interband transitions, which are neglected in the present Drude description of the silver nanowires.

In order to obtain further insight into the azimuthal modes and the excitation amplitude dynamics, we computed the EELS for a long silver nanowire with length $L = 1.2$ μm and radius $R = 15$ nm numerically via the DGTD solver using Eq. (5) for the trajectories indicated by the red dots [see Fig. 2(g)] and display the results in Fig. 3(g). We observe clear standing-wave-like fundamental modes in the lower energy range and well-defined higher-order azimuthal modes right below the unscreened surface plasmon energy value $\omega/\omega_{\mathrm{p}} = 1/\sqrt{2}$. In these computations, we used a shorter wire than in the experiment, since we found it to be sufficiently long to obtain a well-defined dispersion relation while keeping the calculation time in a reasonable regime. The electron velocity is set to $v = 0.4c$ as in Fig. 2. When comparing experiments and simulations, we found that the EELS maps match qualitatively with each other [cf. Figs. 3(a) and 3(g), respectively].

As a first step, we compute the spatial Fourier transform of the EELS map from Fig. 3(g) in order to obtain the dispersion relation of the SPPs (i.e., $\hbar\omega$ energy and k momentum diagram), which can be compared with the analytical dispersion relation for an infinite cylinder [47]. As shown in Fig. 3(h), the computed dispersion relation of the SPPs matches the dispersion of an infinite cylinder (pink curve) calculated using a local Drude model, as expected for a sufficiently long nanowire. Since the radius of the wire is small ($R = 15$ nm), the dispersion curve is far from the dispersion relation of a planar silver/air interface (blue curve). As a matter of fact, the latter case corresponds to the limiting situation when the radius of the cylinder is infinite, or when the characteristic size of the excitations is much smaller than the curvature of the structure. Therefore, in the $Rk \to \infty$ limit, all lines converge to the surface plasmon energy value $\omega/\omega_{\mathrm{p}} = 1/\sqrt{2}$, at least when neglecting the screening effects of interband transitions in the material properties. The fundamental modes ($n = 0$) are clearly visible with very well-defined energy and parallel momentum [see black crosses indicating the maxima of the

colormap in Fig. 3(h)]. Moreover, the higher-order mode with $n = 1$ is also visible in the dispersion relation in Fig. 3(h). Additionally, at energy $\omega/\omega_p \sim 0.6$ [shown in Fig. 3(g)] for trajectories close to the termination of the wire, there are further features in the EEL spectra (indicated by red arrows), which are attributed to the geometrical shape of the caps and the fact that despite being a long wire, it is still finite in length. In our case, the terminations of the wire were simulated with hemispherical caps, and the bright horizontal lines around the $n = 1$ mode in the dispersion relation of Fig. 3(h) are related to the localized Mie resonances associated with these caps. For further clarification, in Sec. S4 in SM Ref. [37], we have superimposed Mie calculations using the MNPBEM toolbox [52] for a full sphere to the EELS map, and this corroborates the origin of these features. Note that the artifacts around $k = 0$ in the dispersion relation originate from the Fourier transform as a sum of the positive EELS signals with a phase factor $e^{ikx} = 1$.

Note that the longer wire in the experiment leads to a better contrast in the experimental dispersion features relative to those in the computations, as the FT of a longer system in real space leads to more localized features in reciprocal space.

Analogous to Fig. 3(c), the theoretical excitation amplitude maps are shown in Fig. 3(i) (without higher-order azimuthal modes) and Fig. 3(j) (with higher-order azimuthal modes). Here, we disentangle the individual contributions of the different modes in order to study the effect of azimuthal SPP modes in the $\tilde{\eta}_r(t)$ map. In Fig. 3(j), we observe a set of horizontal lines that are absent in Fig. 3(i), which indicates the presence of azimuthal modes in the simulated results of Fig. 3(j). This is further corroborated by the fact that these lines appear independently of the electron path along the wire, indicating that the corresponding modes do not propagate along the wire but instead circle around it. Specifically, as demonstrated in Fig. S1 of SM Ref. [37], we compute the $\tilde{\eta}_r(t)$ map by applying different energy filters to the original EEL spectra of Fig. 3(g). Remarkably, when including the entire map (i.e., including horizontal lines of Fig. 3(g) above $\omega/\omega_p \sim 0.6$ and below the surface plasmon energy $\omega/\omega_p = 1/\sqrt{2}$), the resulting features in Fig. 3(j) are those of a set of azimuthal waves that are closely spaced in energy and therefore yield interference beating effects, which is also observed in the experimental $\tilde{\eta}_r(t)$ map in Fig. 3(c). However, a detailed experimental retrieval of higher-order azimuthal modes cannot be accomplished due to the presence of imperfections on the sample surface and the substrate, which broaden their fingerprints [see Fig. 3(a)] [53].

We find a very good qualitative agreement between the measured and computed excitation amplitude dynamics [see Figs. 3(c) and 3(j)]. In both cases, well-defined features with large excitation amplitudes emerge symmetrically from the nanowire caps and propagate toward the center. Although the nanowire is relatively long, its finite length gives rise to distinct enhancements in the electron energy-loss signal. The slopes characterizing the main features differ between experiment and simulation due to the different radii of the respective nanowires, which result in distinct dispersion relations. To account for this effect, we performed additional simulations for a wire with a larger radius of $R = 30$ nm, as shown in Fig. S4 of SM Ref. [37].

By comparing $\tilde{\eta}_r(t)$ in Fig. 3(j) along the x axis and the electric near field Fig. 2(i) for the same time axis, we notice that these two plots share their main features. This indicates that $\tilde{\eta}_r(t)$ is closely related to the near-field profile of the plasmonic excitations given by $E_z^{\mathrm{ind}}(\mathbf{r}_s, t)$. Moreover, in Fig. 3(j) (black dashed line) and Fig. 2(i) (white dashed line), we display the $t_1 + t_3$ time for each electron trajectory x_0. We notice that the bright propagating features in both plots match well with the round-trip time, allowing us to calculate the round-trip time $t_1 + t_3$ directly from the experimental EELS data, thereby fixing the group velocity of the propagating SPP wave packet.

This effect can be understood by recalling that SPP fields are evanescent and remain localized near the nanowire. A short SPP pulse launched at the excitation point propagates along the wire, reflects partially at the end cap, and returns after a delay corresponding to the round-trip time. When this reflected pulse reaches the initial position, it adds to the original excitation, producing a sharp increase in $\tilde{\eta}_r(t)$, as indicated by Eq. (7). This qualitatively explains why the bright propagating features in Figs. 3(j) and 2(i) coincide with the round-trip time of the SPP wave packet.

Specifically, for the experimental excitation amplitude in Fig. 3(c), we obtain the slope of the bright feature to be propagating at $0.38c$, indicating that the group velocity of the SPP wave packets in the experiments is $v_G \approx 0.76c$, while we obtain $v_G \approx 0.7c$ in the computation for a wire with the same radius (for further details, see Fig. S6(d) in SM Ref. [37]). In this case, the computed values of the slope and the experimentally obtained ones show slight differences, as we are using a Drude model for the computations and neglect the screening effects associated with interband transitions. Note that the maps $\tilde{\eta}_r(t)$ in Figs. 3(c) and 3(j) do not change for different electron velocities since the dispersion relation of the SPPs does not depend on the excitation velocity. However, while the SPP profile remains qualitatively the same for different kinetic energies of the electron, the electric field profile at the electron position nonetheless changes [see Fig. S8(d) in SM Ref. [37]].

Moreover, in Sec. S8 of SM Ref. [37] (see also Refs. [54,55] therein), we address the effect of the substrate on the EELS measurements, indicating the presence of excited guided modes in the substrate. Because the silicon nitride membrane is rather thin and, in the spectral region considered, exhibits a rather low refractive index ($n \approx 2$), its influence on the dispersion of the metal cylinder is weak and can be neglected. This is consistent with Fig. 3(b), where the analytical dispersion (pink) lies slightly above the experimental result (color map), indicating a minor substrate and surface-contamination effect. This weak coupling is further reduced by the small contact area between the curved nanowire and the flat substrate. A membrane with a higher refractive index would provide stronger field confinement and support more guided modes, thereby enhancing the coupling to the metal cylinder and eventually leading to a stronger modification of the SPP dispersion relation. Additionally, Fig. S4 in SM

Ref. [37] depicts the fields on the surface of a finite wire at two particular instances of time after the electron has passed by, where the azimuthal SPP modes $n > 0$ combine with fundamental SPP modes with $n = 0$, thereby creating tilted wavefronts of the electric field. This indicates the presence of azimuthal modes with nontrivial azimuthal dynamics around the wire in addition to the fundamental modes that only travel along the nanowire without azimuthal dependence.

D. Fabry-Pérot modes and density of optical states

Inside the wire, there are two main loss mechanisms that are directly responsible for the observed electron energy loss: Ohmic losses associated with the imaginary part of the dielectric function of the metal, and radiative losses. Analyses of the EELS peak widths [shown in Fig. S2(c) [37]] for experimentally measured spectra with an aloof trajectory near the wire cap [see the inset in Fig. S2(c) [37]] and for a simulated structure (see Fig. S5(d) in SM Ref. [37]), clearly show that in both cases, the widths of all peaks are larger than the intrinsic Drude damping of $\hbar\gamma = 21$ meV (see green dashed line). Such an effect has previously been reported [56], and it is a tell-tale of the combination of radiative and nonradiative losses, as observed in Fig. S2d in Ref. [37], where different SPP modes exhibit well-defined spatial profiles and manifest a partial drop in the EELS signal at the caps of the nanowire. This suggests that, at the wire caps, a part of the electromagnetic energy of the modes gets reflected into the nanowire and a part is transmitted out of the nanowire, i.e., converted into radiation. Interestingly, the spatial profiles of the modes resemble those of Fabry-Pérot cavities [57][see Fig. S10b in SM Ref. [37], where the profile of the modes outside the cavity exponentially decay, cf. the black dashed lines in the left-hand side of Figs. 3(e) and S2(d) in SM Ref. [37]].

To theoretically understand the temporal characteristics of the propagating SPP dynamics, we perform a more detailed discussion within a simplified toy model in Sec. S9 of SM Ref. [37], where the full-time evolution is decomposed into a superposition of different SPP modes in plane wave form $e^{i(k_j x-\omega_j t)}$ for SPP mode j. This model sheds light on how the different SPP modes propagate collectively as SPP wave packets in the wire and allows us to define a group velocity v_G. Furthermore, due to the superposition of all modes, we identify how satellites of the first plasmonic wavefront with smaller magnitude move at a slower speed to the left, as shown in Fig. S11(a).

The EELS signatures for each mode in Figs. 3(a) and 3(g) exhibit the shape of standing waves of the form $\cos^2(k_j x)$ located at $\omega = \omega_j$ and are confined to the wire of length L. To model such a behavior, we use $\psi_{\text{standing}}(x,t) = \sum_j \hat{A}_j \cos^2(k_j x) e^{-i\omega_j t}$, with $\hat{A}_j$ being the amplitude for mode j [as shown in Fig. 3(k)], and the corresponding results agree well with $\tilde{\eta}_r(t)$ shown in Fig. 3(i) without higher-order azimuthal modes. This suggests that the SPP modes of order $n = 0$ are responsible for the main features in the excitation amplitude maps for the $R = 15$ nm wire.

Incidentally, such a toy model is related to the local density of optical states (LDOS) $\rho(\omega, x) = \sum_j \hat{A}_j \cos^2(k_j x)\,\delta(\omega - \omega_j)$, where EELS and LDOS have been shown to share some common features [43–45]. Within this description, the Fourier transform in the time domain of the LDOS $\rho(t, x)$ is, therefore, comparable to the excitation amplitude map $\tilde{\eta}_r(t)$ in the time domain of Figs. 3(c) and 3(j). As observed in Fig. 3(k), we can directly relate $\rho(t, x)$ with the round-trip time $t_1 + t_3$. We provide more details in Sec. S9 and Fig. S11.

Therefore, the description of the SPP modes with well-defined $\{k_j, \omega_j\}$ reproduces the main features of the $\tilde{\eta}_r(t)$ map, thus characterizing both, the group velocity and the round-trip time. Further, via v_G and Eq. (8) we obtain the return time t_R. This result can be generalized for any long wire: for known wire length L, the values of $k_j = j\pi/L$ are also known, which in turn are related to ω_j through the dispersion relation of an infinitely long wire. Thereby, v_G together with the round-trip time and t_R are fixed with the prescription introduced above.

III. METHODS

A. Sample preparation

Materials: Silver nitrate (99%), ethylene glycol (99.8%), poly-(vinylpyrrolidone) (Mw = 40000), tetraethyl orthosilicate (TEOS), sodium chloride, ammonia solution (28 wt %), and absolute ethanol were purchased from Aldrich. All chemicals were used without further purification.

Silver nanowires (AgNWs) of approximately 1–3 μm length and 30 nm width were synthesized according to our previous report [58], which was adapted from a method developed by Hu *et al.* [59]. In short, 34 mL poly-(vinylpyrrolidone) solution (1.47 mM in ethylene glycol) was heated to 160 °C, then 40 μL sodium chloride solution (also dissolved in ethylene glycol, 0.1 M) was added. After stirring for 1 min, 6 mL silver nitrate solution (in ethylene glycol, 0.67 M) was added at a rate of 10 μL/s until the mixture appeared turbid. Once turbid, the rest of the silver nitrate solution was added rapidly. The mixture was stirred at 160°C for 30 mins, then cooled to room temperature and centrifuged. The supernatant was discarded, and the silver nanowires were redispersed in ethanol. The dispersion was stored at 4 °C until use. Samples of Ag nanowires were prepared for characterization by depositing a drop of the dispersion on silicon nitride supported TEM grids of 15 nm thickness (purchased from Plano) and letting them dry at room temperature.

B. Electron microscopy

STEM imaging and electron energy-loss spectroscopy were performed on the Nion aberration-corrected high-energy resolution monochromated EELS-STEM (HERMES) system [60] at Humboldt-Universität zu Berlin operated at 30 kV, 60 kV, and 200 kV accelerating voltage, equipped with a Dectris ELA direct detector. Additional nanowires ($N > 10$) were measured under comparable conditions, and a representative subset is highlighted in this manuscript. The energy resolution of the EELS acquisition was measured using FWHM of the zero-loss peak (ZLP) and was found to be between 12–21 meV depending on accelerating voltage. The convergence semiangle was 10 mrad. EELS was performed using a 5–20 nm pixel size with a maximum field of view of 5 μm. All analysis of the microscopy data was carried out using the open-source Python package HyperSpy [61]. Richardson-Lucy deconvolution was employed for ZLP removal within the HyperSpy environment. During EELS acquisition, the

beam current was $I = 5$–50 pA, corresponding to a mean interarrival time $\Delta t \approx e/I \sim 3$–$30$ ns, which is orders of magnitude longer than both the femtosecond electron–sample interaction window and the plasmon dephasing times. Events are therefore independent (single-electron regime).

C. Numerical simulation

The DGTD finite-element approach [33] was used to simulate the electromagnetic problem of a silver nanowire excited by an electron beam. In this approach, a polynomial spatial interpolation basis of adjustable order (typically third or fourth order) on an unstructured tetrahedral mesh [see Fig. S7 in Ref. [37] (see also Ref. [62] therein)] is combined with a low-storage Runge-Kutta time integrator (typically fourth order), thereby providing an efficient solver for the time-dependent Maxwell's equations:

$$\partial_t \mathbf{H}(\mathbf{r}, t) = -\mu_0^{-1}\mu^{-1}(\mathbf{r})\,\nabla \times \mathbf{E}(\mathbf{r}, t), \tag{9a}$$

$$\partial_t \mathbf{E}(\mathbf{r}, t) = \varepsilon_0^{-1}\varepsilon^{-1}(\mathbf{r})\,[\nabla \times \mathbf{H}(\mathbf{r}, t) - \mathbf{j}(\mathbf{r}, t)]. \tag{9b}$$

Here, $\mathbf{j}$ is the total current density that encompasses any currents associated with the excitation source and dispersive polarization currents (see Sec. S7 in SM Ref. [37] for further technical details). The resulting method is memory-efficient and particularly well-suited for calculating broadband spectra.

Due to the symmetry of the nanowire, we only considered trajectories along a line on the right half side of the nanowire with respect to the *yz*-plane, which cuts through the middle of the nanowire [see Fig. 2(e)]. At the same time, the cylindrical symmetry regarding around the long axis of the finite cylinder means that a rotation of the trajectories along the long axis will give the same EELS maps [31].

Electron source. In particular, the electron source is implemented as a Gaussian charge distribution of the form

$$\rho(\mathbf{r}) = -\frac{e}{\sigma_e^3\sqrt{\pi^3}} \mathrm{e}^{-r^2/\sigma_e^2}, \tag{10}$$

with width $\sigma_e = 5\,\mathrm{nm}$. This choice essentially prevents numerical artifacts arising from the implementation of a point-charge particle moving inside the nanowire. The induced electric fields $\mathbf{E}^{\mathrm{ind}}$ along the electron trajectory are recorded in the time domain, and subsequently, an on-the-fly Fourier transform within DGTD allows the conversion of the simulation data to the frequency domain. EEL spectra for the nanowire are then computed in a post-processing step according to Eq. (5).

No-recoil approximation. By integrating $\Gamma_{\mathrm{EELS}}(\omega)$ following Eq. (4), we calculated the total energy loss ΔE of the electron to the various plasmonic excitations, which is much smaller than the kinetic energy of the electrons. Additionally, the total momentum transfer from the electron to the nanowire is $\hbar k \approx \hbar\omega_{\mathrm{loss}}/v \ll m_e v$, where m_e is the mass of the electron. Therefore, the no-recoil approximation [31] is adopted for the numerical computations.

IV. CONCLUSION

In summary, we have introduced a combined experimental-theoretical approach for a time-dependent perspective on EELS signals from plasmonic nanostructures. This time-dependent perspective allows for identifying and unraveling the dynamics of different plasmonic excitations and leads to deeper insights into the underlying physics. In particular, our study highlighted the role of propagating fundamental surface plasmon polariton wave packets in thin silver nanowires that move at specific group velocities, which depend only on the radius and material properties of the wire. Further, we were able to quantitatively determine the group velocity of these wave packets and correlate this with the measured EELS. In addition, we have been able to estimate the time it takes to form such SPP wave packets. These wave packets bounce back and forth in the wire and lead to the Fabry-Pérot-like modes providing resonance conditions, which, in turn, enhance the electron-light interaction and result in the EELS features that could be measured/computed. Moreover, despite the fact that the thin wire represents an almost one-dimensional system, we have identified the effects of higher-order azimuthal surface plasmon polaritons in both DGTD-simulated and measured EEL data, as well as in the probability amplitude dynamics.

This has been accomplished by going beyond the study of the spatiospectral information obtained via standard EELS maps. In fact, the Fourier transform of the coupling coefficient (computed via EELS signal) sheds light on the electron-photon interaction probability mechanisms in the time domain, and this approach can be applied to any material configuration. For instance, such a comprehensive understanding of the temporal evolution of plasmonic excitations opens a route for controlling the losses in plasmonic systems. Specifically, while the overall result of the interaction of the electron with the plasmonic nanostructure is an energy loss, the oscillatory character of the electromagnetic fields provides a local/differential gain that can be exploited via more complex configurations than those we have considered in the present work, i.e., by properly "surfing" on the SPP dynamics. In doing so, our time-dependent perspective provides a refined view of the losses in metals that can be utilized to design better plasmonic resonators [63] for chemical applications, plasmonic sensors for spectroscopy, and controlling coherent effects [64].

ACKNOWLEDGMENTS

A.E., T.K., K.B., and C.T.K. acknowledge funding by the Deutsche Forschungsgemeinschaft (DFG) in the framework of the Collaborative Research Center (CRC) 951 (Project ID 182087777). H.C.N. acknowledges funding by the DFG, Project No. 449639588 (NE 2491/2-1) in the framework of the DFG Priority Programme 2244: 2D Materials – Physics of van der Waals [hetero]structures. K.B. acknowledges funding by the Deutsche Forschungsgemeinschaft (DFG) in the framework of the CRC 1636 (Project ID 510943930 - Project No. A06) and the CRC 1375 (Project ID 398816777 - Project No. A06). C.T.K. acknowledges funding by DFG in Projekt CAPTURE (Project ID 541930824).

A.E. initiated the study. K.B. and C.T.K. supervised the research. W.Z. carried out the DGTD computations and contributed to the analysis of the experimental results and the theoretical analysis. A.R.E. contributed to the theoretical analysis and coordinated the collaboration between the theoretical

and the experimental teams. A.E. carried out the experiments and experimental EELS data processing. B.H. supported in the operation of the microscope. H.C.N. contributed to the experimental data processing. T.K. helped with the DGTD computations and advised on the theoretical analysis. H.H. and Y.L. provided the Ag nanowire samples. All authors participated in the discussion of the results and the writing of the manuscript.

DATA AVAILABILITY

The data that support the findings of this article are not publicly available upon publication because it is not technically feasible and/or the cost of preparing, depositing, and hosting the data would be prohibitive within the terms of this research project. The data are available from the authors upon reasonable request.

[1] M. Kauranen and A. V. Zayats, Nonlinear plasmonics, Nature Photon **6**, 737 (2012).
[2] X. Xu, H. Li, D. Hasan, R. S. Ruoff, A. X. Wang, and D. Fan, Near-field enhanced plasmonic-magnetic bifunctional nanotubes for single cell bioanalysis, Adv. Funct. Mater. **23**, 4332 (2013).
[3] B. Sharma, R. R. Frontiera, A.-I. Henry, E. Ringe, and R. P. Van Duyne, Sers: Materials, applications, and the future, Mater. Today **15**, 16 (2012).
[4] S. I. Bozhevolnyi, Plasmonic nano-guides and circuits, in *Plasmonics and Metamaterials* (Optica Publishing Group, Rochester, New York, 2008), p. MWD3.
[5] H.-K. Yu, B.-D. Liu, W.-L. Wu, and Z.-Y. Li, Surface plasmaons enhanced light-matter interactions, Acta Phys. Sin. **68**, 149101 (2019).
[6] J. N. Anker, W. P. Hall, O. Lyandres, N. C. Shah, J. Zhao, and R. P. Van Duyne, Biosensing with plasmonic nanosensors, Nat. Mater. **7**, 442 (2008).
[7] F. Arcadio, L. Noel, D. Prete, D. Maniglio, M. Seggio, O. Soppera, N. Cennamo, A. Bossi, and L. Zeni, Soft molecularly imprinted nanoparticles with simultaneous lossy mode and surface plasmon multi-resonances for femtomolar sensing of serum transferrin protein, Sci. Rep. **13**, 11210 (2023).
[8] N. Jo and Y.-B. Shin, Enhancing biosensing sensitivity of metal nanostructures through site-selective binding, Sci. Rep. **10**, 1024 (2020).
[9] R. Liu, Z.-K. Zhou, Y.-C. Yu, T. Zhang, H. Wang, G. Liu, Y. Wei, H. Chen, and X.-H. Wang, Strong light-matter interactions in single open plasmonic nanocavities at the quantum optics limit, Phys. Rev. Lett. **118**, 237401 (2017).
[10] A. Gonzalez-Tudela, A. Reiserer, J. García-Ripoll, and F. García-Vidal, Light–matter interactions in quantum nanophotonic devices, Nat. Rev. Phys. **6**, 166 (2024).
[11] S. Slussarenko and G. Pryde, Photonic quantum information processing: A concise review, Appl. Phys. Rev. **6**, 041303 (2019).
[12] D. Smirnova and Y. Kivshar, Multipolar nonlinear nanophotonics, Optica **3**, 1241 (2016).
[13] W. L. Barnes, A. Dereux, and T. W. Ebbesen, Surface plasmon subwavelength optics, Nature (London) **424**, 824 (2003).
[14] B. Wang, P. Yu, W. Wang, X. Zhang, H.-C. Kuo, H. Xu, and Z. Wang, High-Q plasmonic resonances: Fundamentals and applications, Adv. Opt. Mater. **9**, 2001520 (2021).
[15] M. Mayer, L. Scarabelli, K. March, T. Altantzis, M. Tebbe, M. Kociak, S. Bals, F. J. García de Abajo, A. Fery, and L. M. Liz-Marzán, Controlled living nanowire growth: Precise control over the morphology and optical properties of AgAuAg bimetallic nanowires, Nano Lett. **15**, 5427 (2015).
[16] M. Rothe, Y. Zhao, G. Kewes, Z. Kochovski, W. Sigle, P. A. van Aken, C. Koch, M. Ballauff, Y. Lu, and O. Benson, Silver nanowires with optimized silica coating as versatile plasmonic resonators, Sci. Rep. **9**, 3859 (2019).
[17] A. Baburin, A. Merzlikin, A. Baryshev, I. Ryzhikov, Y. Panfilov, and I. Rodionov, Silver-based plasmonics: Golden material platform and application challenges, Opt. Mater. Express **9**, 611 (2019).
[18] R. F. Egerton, *Electron Energy-Loss Spectroscopy in the Electron Microscope* (Springer New York, NY, 2011), pp. XII, 491.
[19] A. Liu, T. Davis, T. Coenen, S. Hari, L. Voortman, Z. Xu, G. Yuan, P. Ballard, A. Funston, and J. Etheridge, Modulation of cathodoluminescence by surface plasmons in silver nanowires, Small **19**, 2207747 (2023).
[20] J. Nelayah, M. Kociak, O. Stéphan, F. J. García de Abajo, M. Tencé, L. Henrard, D. Taverna, I. Pastoriza-Santos, L. M. Liz-Marzán, and C. Colliex, Mapping surface plasmons on a single metallic nanoparticle, Nat. Phys. **3**, 348 (2007).
[21] M. Bosman, V. Keast, M. Watanabe, A. Maaroof, and M. Cortie, Mapping surface plasmons at the nanometre scale with an electron beam, Nanotechnology **18**, 165505 (2007).
[22] C. Colliex, M. Kociak, and O. Stéphan, Electron energy loss spectroscopy imaging of surface plasmons at the nanometer scale, Ultramicroscopy **162**, A1 (2016).
[23] G. Ruthemann, Diskrete energieverluste mittelschneller elektronen beim durchgang durch dünne folien, Ann. Phys. **437**, 113 (1948).
[24] R. Vincent and J. Silcox, Dispersion of radiative surface plasmons in aluminum films by electron scattering, Phys. Rev. Lett. **31**, 1487 (1973).
[25] H. Watanabe, Experimental evidence for the collective nature of the characteristic energy loss of electrons in solids–studies on the dispersion relation of plasma frequency–, J. Phys. Soc. Jpn. **11**, 112 (1956).
[26] D. Rossouw, M. Couillard, J. Vickery, E. Kumacheva, and G. Botton, Multipolar plasmonic resonances in silver nanowire antennas imaged with a subnanometer electron probe, Nano Lett. **11**, 1499 (2011).
[27] D. Rossouw and G. Botton, Plasmonic response of bent silver nanowires for nanophotonic subwavelength waveguiding, Phys. Rev. Lett. **110**, 066801 (2013).
[28] X. Zhou, A. Hörl, A. Trügler, U. Hohenester, T. Norris, and A. Herzing, Effect of multipole excitations in electron energy-loss spectroscopy of surface plasmon modes in silver nanowires, J. Appl. Phys. **116**, 223101 (2014).
[29] D. Nabben, J. Kuttruff, L. Stolz, A. Ryabov, and P. Baum, Attosecond electron microscopy of sub-cycle optical dynamics, Nature (London) **619**, 63 (2023).

[30] R. H. Ritchie, Plasma losses by fast electrons in thin films, Phys. Rev. **106**, 874 (1957).

[31] F. J. García de Abajo, Optical excitations in electron microscopy, Rev. Mod. Phys. **82**, 209 (2010).

[32] C. H. Chen and J. Silcox, Detection of optical surface guided modes in thin graphite films by high-energy electron scattering, Phys. Rev. Lett. **35**, 390 (1975).

[33] K. Busch, M. König, and J. Niegemann, Discontinuous Galerkin methods in nanophotonics, Laser Photonics Rev. **5**, 773 (2011).

[34] P. E. Stamatopoulou, W. Zhao, A. Rodríguez Echarri, N. A. Mortensen, K. Busch, C. Tserkezis, and C. Wolff, Electron beams traversing spherical nanoparticles: Analytic and numerical treatment, Phys. Rev. Res. **6**, 013239 (2024).

[35] B. Schröder, T. Weber, S. V. Yalunin, T. Kiel, C. Matyssek, M. Sivis, S. Schäfer, F. von Cube, S. Irsen, K. Busch, C. Ropers, and S. Linden, Real-space imaging of nanotip plasmons using electron energy loss spectroscopy, Phys. Rev. B **92**, 085411 (2015).

[36] P. B. Johnson and R. W. Christy, Optical constants of the noble metals, Phys. Rev. B **6**, 4370 (1972).

[37] See Supplemental Material at http://link.aps.org/supplemental/10.1103/gpqj-4v29 for the technical details and additional information regarding our study. Specifically, we give a derivation of the temporal analysis of EELS, address the surface plasmon polariton dispersion relation of infinite nanowires, expand the technical formalism to solve the electromagnetic problem numerically via the DGTD Maxwell solver, and provide further details about the characteristics of the surface plasmon polariton modes in silver long nanowires. Finally, the influence of the substrate is addressed.

[38] A. Rodríguez Echarri, W. Zhao, K. Busch, and F. J. García de Abajo, Relativistic electron energy-loss spectroscopy in cylindrical waveguides and holes, Phys. Rev. B **111**, 205436 (2025).

[39] V. Lucarini, J. Saarinen, K. Peiponen, and E. Vartiainen, *Kramers-Kronig Relations in Optical Materials Research* (Springer, Berlin, Heidelberg, 2005).

[40] J. L. Walsh, The Cauchy-Goursat theorem for rectifiable Jordan curves, Proc. Natl. Acad. Sci. USA **19**, 540 (1933).

[41] V. G. Kravets, A. V. Kabashin, W. L. Barnes, and A. N. Grigorenko, Plasmonic surface lattice resonances: A review of properties and applications, Chem. Rev. **118**, 5912 (2018).

[42] R. H. Ritchie and A. Howie, Inelastic scattering probabilities in scanning transmission electron microscopy, Philos. Mag. A **58**, 753 (1988).

[43] F. J. García de Abajo and M. Kociak, Probing the photonic local density of states with electron energy loss spectroscopy, Phys. Rev. Lett. **100**, 106804 (2008).

[44] U. Hohenester, H. Ditlbacher, and J. R. Krenn, Electron-energy-loss spectra of plasmonic nanoparticles, Phys. Rev. Lett. **103**, 106801 (2009).

[45] A. Losquin and M. Kociak, Link between cathodoluminescence and electron energy loss spectroscopy and the radiative and full electromagnetic local density of states, ACS Photonics **2**, 1619 (2015).

[46] N. Talebi, W. Sigle, R. Vogelgesang, M. Esmann, S. F. Becker, C. Lienau, and P. A. van Aken, Excitation of mesoscopic plasmonic tapers by relativistic electrons: Phase matching versus eigenmode resonances, ACS Nano **9**, 7641 (2015).

[47] J. C. Ashley and L. C. Emerson, Dispersion relations for nonradiative surface plasmons on cylinders, Surf. Sci. **41**, 615 (1974).

[48] A. Polman, M. Kociak, and F. J. García de Abajo, Electron-beam spectroscopy for nanophotonics, Nat. Mater. **18**, 1158 (2019).

[49] D. B. Williams and C. B. Carter, *Transmission Electron Microscopy* (Springer, New York, NY, 2009).

[50] J. M. Pitarke, V. M. Silkin, E. V. Chulkov, and P. M. Echenique, Theory of surface plasmons and surface-plasmon polaritons, Rep. Prog. Phys. **70**, 1 (2007).

[51] S. Zhang, H. Wei, K. Bao, U. Håkanson, N. J. Halas, P. Nordlander, and H. Xu, Chiral surface plasmon polaritons on metallic nanowires, Phys. Rev. Lett. **107**, 096801 (2011).

[52] U. Hohenester and A. Trügler, MNPBEM – A Matlab toolbox for the simulation of plasmonic nanoparticles, Comput. Phys. Commun. **183**, 370 (2012).

[53] Note that we use the same experimental setup both in Fig. 3 and Fig. S2 but with different energy ranges and consequently different energy sampling δE. Specifically, in Fig. 3 we have $\delta E = 0.003\,\text{eV}$ while in Fig. S2 we have $\delta E = 0.006\,\text{eV}$.

[54] H. Wei, D. Pan, S. Zhang, Z. Li, Q. Li, N. Liu, W. Wang, and H. Xu, Plasmon waveguiding in nanowires, Chem. Rev. **118**, 2882 (2018).

[55] K. Luke, Y. Okawachi, M. R. E. Lamont, A. L. Gaeta, and M. Lipson, Broadband mid-infrared frequency comb generation in a Si_3N_4 microresonator, Opt. Lett. **40**, 4823 (2015).

[56] V. Mkhitaryan, K. March, E. Tseng, X. Li, L. Scarabelli, L. M. Liz-Marzán, S.-Y. Chen, L. H. G. Tizei, O. Stéphan, J.-M. Song, M. Kociak, F. J. García de Abajo, and A. Gloter, Can copper nanostructures sustain high-quality plasmons? Nano Lett. **21**, 2444 (2021).

[57] B. E. A. Saleh and M. C. Teich, Guided-wave optics, in *Fundamentals of Photonics*, edited by J. W. Goodman, B. E. A. Saleh, and M. C. Teich (John Wiley & Sons, Ltd, 1991), Chap. 7, p. 238.

[58] M. Rothe, Y. Zhao, J. Müller, G. Kewes, C. T. Koch, Y. Lu, and O. Benson, Self-assembly of plasmonic nanoantenna–waveguide structures for subdiffractional chiral sensing, ACS Nano **15**, 351 (2021).

[59] M. Hu, J. feng Gao, Y. Dong, S. Yang, and R. K. Li, Rapid controllable high-concentration synthesis and mutual attachment of silver nanowires, RSC Adv. **2**, 2055 (2012).

[60] O. L. Krivanek, T. C. Lovejoy, M. F. Murfitt, G. Skone, P. E. Batson, and N. Dellby, Towards sub-10 meV energy resolution STEM-EELS, J. Phys.: Conf. Ser. **522**, 012023 (2014).

[61] F. de la Peña, E. Prestat, J. Lähnemann, V. T. Fauske, P. Burdet, P. Jokubauskas, T. Furnival, C. Francis, M. Nord, T. Ostasevicius, K. E. MacArthur, D. N. Johnstone, M. Sarahan, J. Taillon, T. Aarholt, pquinn dls, V. Migunov, A. Eljarrat, J. Caron, T. Nemoto, *et al.*, hyperspy/hyperspy: V2.3.0 (v2.3.0), Zenodo (2025), https://doi.org/10.5281/zenodo.14956374.

[62] C. Geuzaine and J.-F. Remacle, Gmsh: A 3-d finite element mesh generator with built-in pre- and post-processing facilities, Int. J. Numer. Methods Eng. **79**, 1309 (2009).

[63] M. R. Gonçalves, H. Minassian, and A. Melikyan, Plasmonic resonators: Fundamental properties and applications, J. Phys. D: Appl. Phys. **53**, 443002 (2020).

[64] N. Talebi, Interaction of electron beams with optical nanostructures and metamaterials: From coherent photon sources towards shaping the wave function, J. Opt. **19**, 103001 (2017).